Supplementary Information

A robust near-field body area network based on coaxially-shielded textile metamaterial

Xia Zhu[1,2], Ke Wu[1,2], Xiaohang Xie[1,2], Stephan W. Anderson[2,3], and Xin Zhang[1,2*]

[1]Department of Mechanical Engineering, Boston University, Boston, MA 02215, United States.
[2]Photonics Center, Boston University, Boston, MA 02215, United States.
[3]Chobanian & Avedisian School of Medicine, Boston University Medical Campus, Boston, MA 02118, United States.

*Corresponding author. E-mail: xinz@bu.edu
Contributing authors: xiaz@bu.edu; wk0305ok@bu.edu; xhxie@bu.edu; sande@bu.edu

Supplementary Note 1. Design strategy for the coaxially-shielded metamaterial.

In the near-field region, magnetic metamaterials are typically composed of resonating loops that form collective resonating modes. The interaction among adjacent unit cells is primarily inductive, dominated by the oscillating magnetic field within each unit cell. The oscillating magnetic field is invariably accompanied by a varying electric field, as dictated by the electromagnetic theorem. Consequently, the magneto-inductive wave in the metamaterial also induces a redistribution and amplification of the electric field in the vicinity of the metamaterial. The amplified electric field can interact with the dielectric and conductive properties of the surrounding media, contributing to the spectral instability and dielectric/conductive loss.

Electric fields are inherently bound by capacitors, with their capacitance value indicating the ability to store electric charge. Hence, a significant self-capacitance in a magnetic metamaterial, which is well-protected and less exposed, is advantageous for achieving desired spectral stability.

Coaxial cables, known for their signal preservation over long distances, are traditionally employed for RF applications, effectively block electromagnetic interference due to their conductive outer layers (shielding layers). Simultaneously, the potential difference between the inner and outer conductors in coaxial cables creates a significant electric field, introducing substantial shunt capacitance. This capacitance is vital for signal integrity and forms the basis for integrating it into the metamaterial's self-capacitance to enhance the robustness of near-field BAN designs.

We observed that directly applying coaxial cable as a conductor to construct conventional helical/spiral resonators does not yield the desired effect (Supplementary Fig. 3), primarily because the well-isolated inner conductor is not sufficiently perceived or excited by the external excitation. Under this configuration, the resonator essentially behaves like a helical resonator with a thicker wire, the current on the outer surface of the outer conductor follows the sinusoidal pattern conventionally found on a helical resonator. By welding the inner and outer conductors together, the inner conductor is thereby electrically exposed, enabling it to participate in resonance, facilitating the desired electric field confinement effect. The equivalent circuit model reveals the current and capacitance distribution within the coaxially-shielded metamaterial and its inter-unit cell coupling mechanism (Supplementary Fig. 4).

The resonance frequency and performance can be affected by several inherent parameters of the adopted coaxial cable, including the conductor material, insulator material, inner conductor radius T_i, insulator thickness T_{ins}, and outer conductor thickness T_o (Supplementary Fig. 5a). The conductor’s conductivity has a direct impact on the ohmic loss and thereby the performance

(Supplementary Fig. 5b). The adopted cable conductor is silver-plated copper, commonly employed in low-loss cable design; it combines silver's high conductivity and resistance to corrosion with copper's lower cost.

The inner and outer conductor are separated by an insulation layer, typically composed of a polymer material with a permittivity value between 2 and 3, constituting a capacitor that provides the electric field confinement while enabling resonance frequency match to NFC despite the unit cell is sub-wavelength. The permittivity of the insulator, inner conductor radius, and insulator thickness all have impact on its capacitance and the performance of the metamaterial (Supplementary Fig. 5c-e). The outer conductor thickness, however, presents negligible effect as it does not significantly alter the layered internal structure (Supplementary Fig. 5f). These parameters are pre-determined by the cable manufacture, and cannot be individually altered to adjust the metamaterial's frequency.

The metamaterial's resonance frequency is optimized through the cable length and the unit cell's covered area. The desired metamaterial should have the highest magnetic field enhancement capability over its coverage area while accommodating practical considerations. For instance, the shorter edges of the metamaterial should be of comparable dimension to the smallest deployable anatomy, namely the calf or forearm, and should be broad enough to cover the sensing nodes. In the meantime, the longer edges of the metamaterial should to be sufficiently long to avoid the excessive usage of more unit cells. The adopted dimension (200 mm × 55 mm) enables a frequency match while striking a balance between magnetic field enhancement and practicality for integration onto existing clothing (Supplementary Fig. 5g-i).

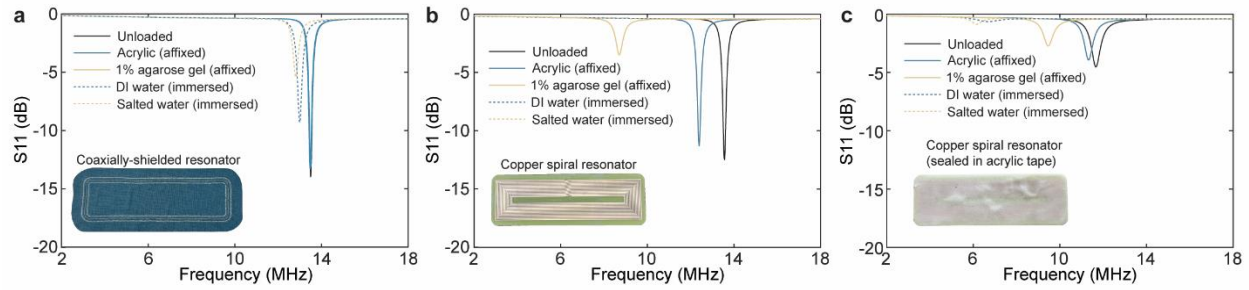

Supplementary Figure 1. Comparison of frequency response between coaxially-shielded resonator and conventional spiral-based resonator. a The coaxially-shielded resonator exhibits frequency shifts of 0, 0.15, 3.72 and 4.96% when affixed to acrylic, affixed to 1 % agarose gel, immersed in deionized (DI) water, and immersed in 0.8% salted water. **b** The conventional copper spiral resonator (milled on 1.5mm-thick FR-4, optimized to the same dimension and frequency as the coaxially-shielded resonator) exhibits frequency shifts of 8.67 and 35.76% when affixed to acrylic and agarose gel, respectively, and fails to maintain detectable resonance when immersed in DI water or saline. **c** After applying two-sided sealing with a 1.5 mm-thick acrylic tape, the copper spiral resonator still exhibits frequency shifts of 3.06, 18.89, 42.84 and 47.15% under these loadings.

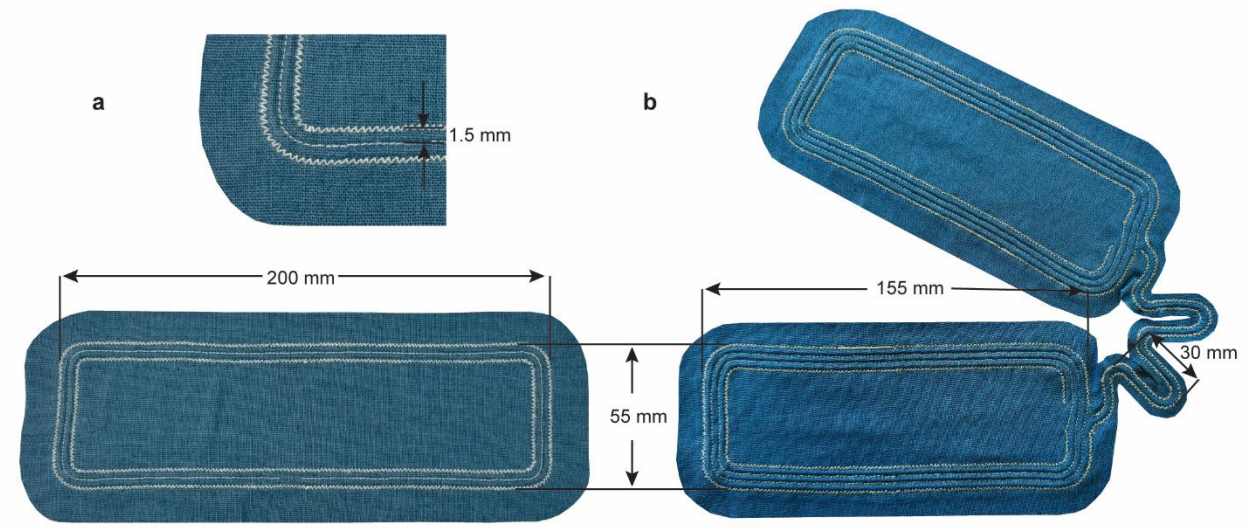

Supplementary Figure 2. Detailed dimensions of the fabricated textile metamaterial patch unit (**a**) and the stretchable textile joint unit (**b**).

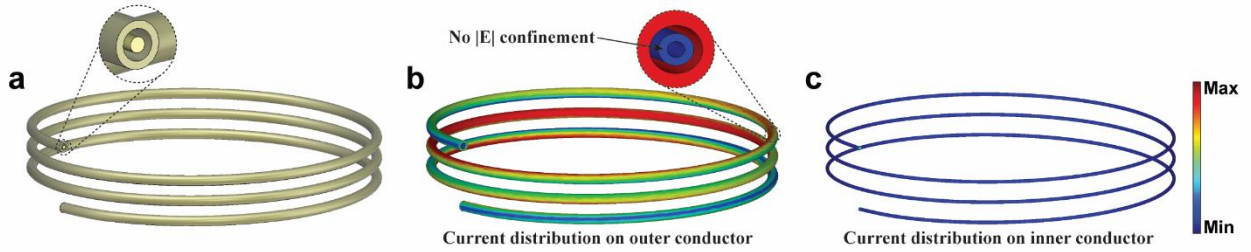

Supplementary Figure 3. **Using coaxial cable to construct helical resonator without welding junction. a** Helical resonator model adopted for simulation. **b** The oscillating current is exclusively distributed on the outer surface of the outer conductor. No desired electric field confinement is observed. **c** No current is observed on the inner conductor due to the shielding effect of the outer conductor.

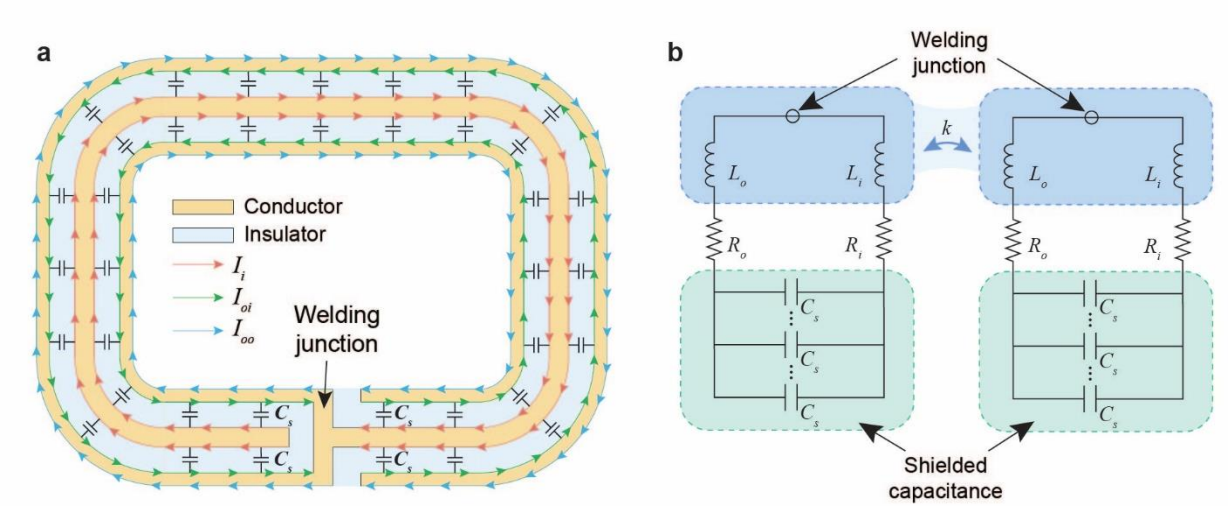

Supplementary Figure 4. **Equivalent circuit model of the coaxially-shielded metamaterial.** **a** Current distribution in the cross-sectional view of the metamaterial unit cell, C_s denotes the structural self-capacitance between the conductor layers. **b** Equivalent circuit diagram reveals the coupling mechanism of the coaxially-shielded metamaterial. L_i and R_i denote the inductance and resistance of the inner conductor, while L_o and R_o represent those of the outer conductor. *k* denotes the inter-unit cell coupling. C_s represent the structural self-capacitance that is confined and isolated within the insulating layer.

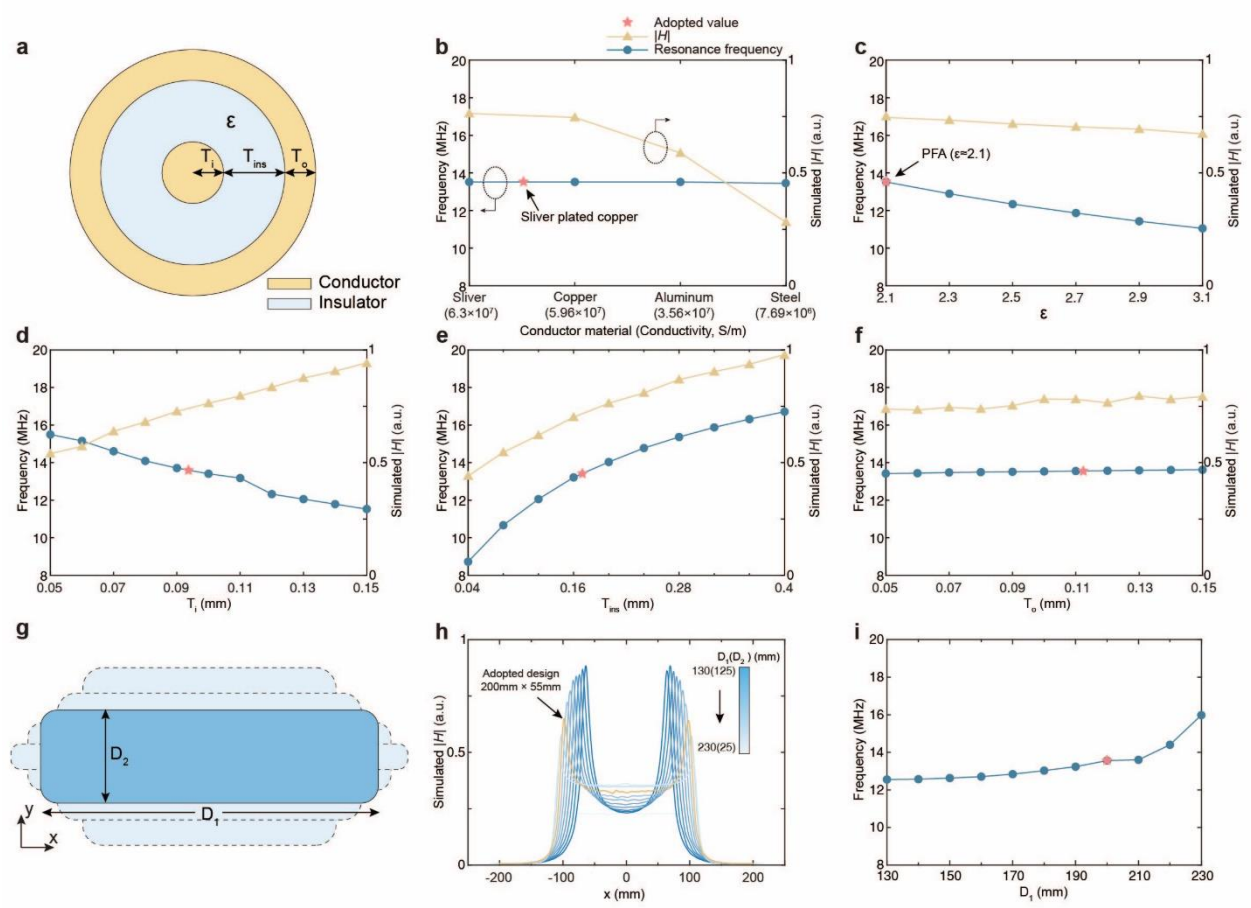

Supplementary Figure 5. **Optimization of the metamaterial design. a** Cross-sectional view of the coaxial cable. **b-f** Impact of the coaxial cable's parameters on the resonance frequency and the magnetic field strength at the center point (x = 0, y = 0) of the metamaterial plane, including conductor material (**b**), insulator material (characterized by ε) (**c**), inner conductor radius T_i (**d**), insulation thickness T_{ins} (**e**), and outer conductor thickness T_o (**f**). **g-i** Impact of the metamaterial's coverage on the magnetic field distribution (**h**) and resonance frequency (**i**) while maintaining the perimeter.

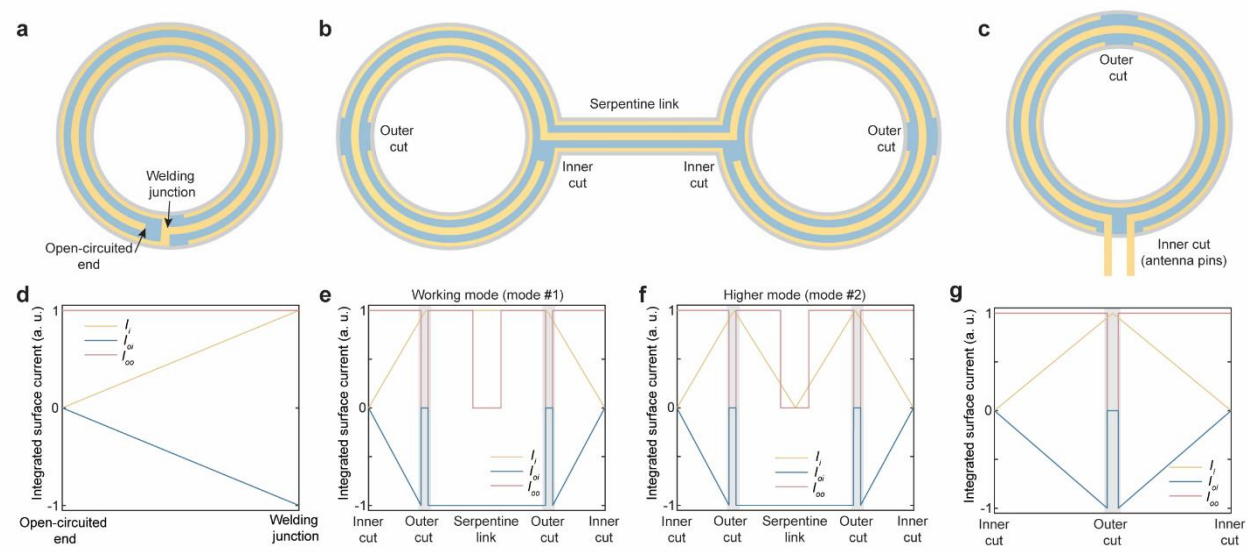

Supplementary Figure 6. Simplified model of the coaxially-shielded metamaterial and antenna. a-c Cross-sectional view of simplified one-turn models of the metamaterial unit cell (**a**), stretchable join units (**b**), and the coaxially-shielded antenna (**c**) while preserving their internal structural topologies. **d-g** Representative integrated surface current along the cable's conductor for the metamaterial unit cell (**d**), the working mode (mode #1 in Figure. 3 of the main text) of the stretchable join unit (**e**), the higher mode (mode #2 in Figure. 3 of the main text) of the stretchable join unit (**f**), and the coaxially-shielded antenna (**g**). The current distributions represent the ideal case of the results derived from simulation and serve to demonstrate the trend of different currents flowing inside the metamaterial/antenna.

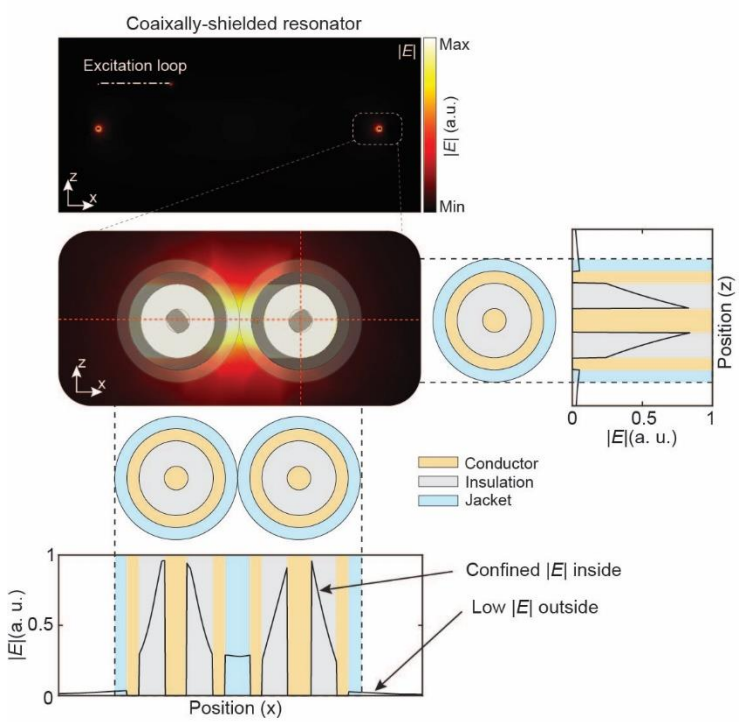

Supplementary Figure 7. **Electric field distribution in proximity to the coaxial cable.** The electric field across the cable's cross-section (red dashed lines) is plotted and precisely mapped to the cable structure, indicating that the majority of the electric field is confined between the two conductor layers.

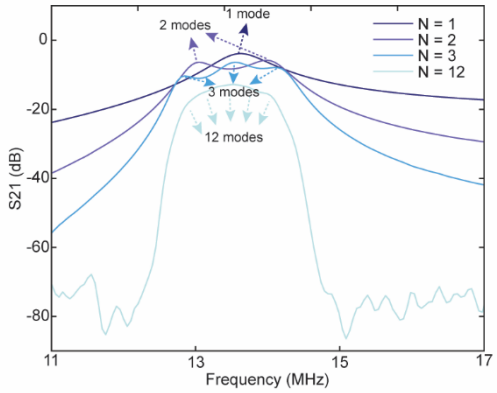

Supplementary Figure 8. Mode splitting of the BAN. Measured transmission coefficient at the two ends of an inline metamaterial array with increasing numbers of unit cells. When more than one unit cell is present in the BAN, the resonant frequency will split into multiple modes (the number of the modes equals to the number of the unit cells), and these modes will merge together and may not exhibit distinguishable individual peaks. The resonant modes will eventually evolve to a wide NFC passband that centers at the frequency of a single unit cell. A 20% inter-unit cell overlap was adopted for this measurement.

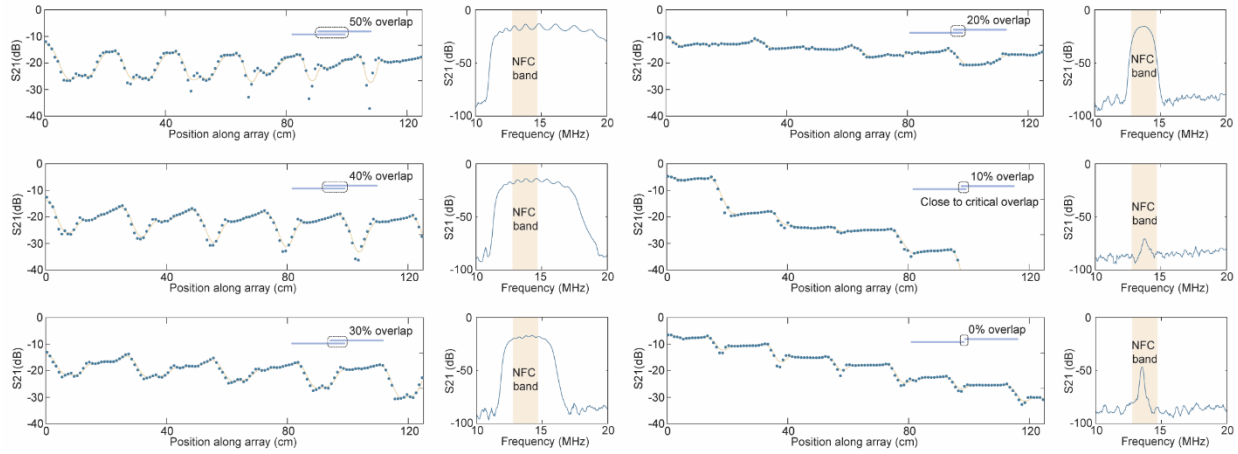

Supplementary Figure 9. Measured magnetic field distribution (characterized by the S21 parameters) along the BAN and the transmission coefficient at the two ends of the BAN with various overlaps. Greater overlap (larger than 25%) yields an excessive bandwidth while induce more predominant field fluctuation along the BAN, while less overlap (smaller than 20%) generate an insufficient bandwidth and the magnetic field decay rapidly along the BAN. 10% overlap maps to the region close to critical overlap, which gives rise to zero inter-unit cell coupling and the fastest decay of magnetic field along the BAN.

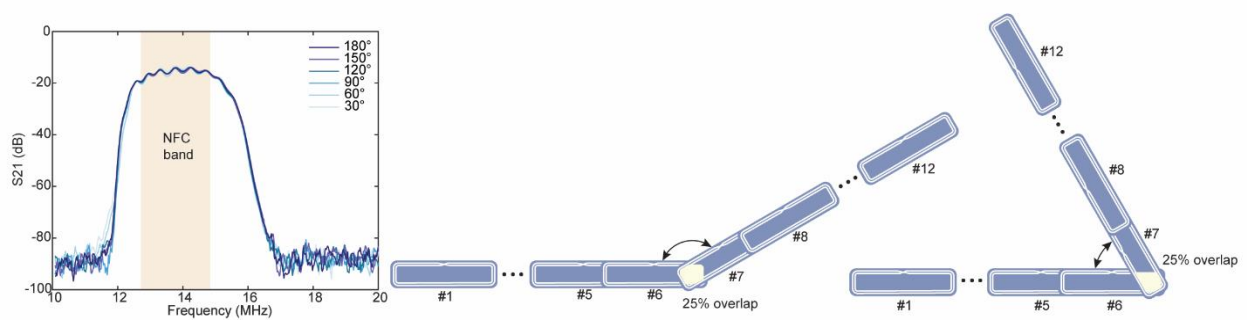

Supplementary Figure 10. Measured transmission coefficient of a 12-unit inline metamaterial array while performing rotation at the intersection of the 6th and 7th unit cell. The overlap between the 6th and 7th unit cells are maintained at 25% during the rotation. The transmission coefficient remains stable regardless of the rotation angle, further demonstrate that the inter-unit cell coupling is dominated by the nearest neighbor coupling while the next nearest neighbor coupling may be neglected. This allows the BAN to be freely routed along different direction.

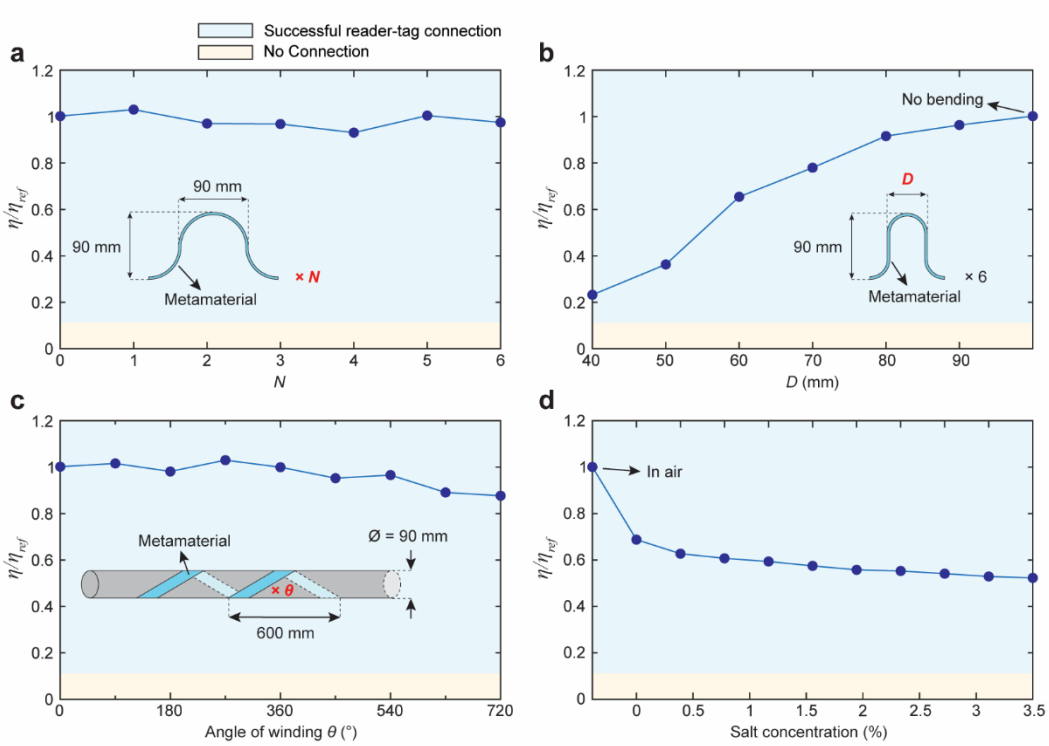

Supplementary Figure 11. **Variation in the power transfer efficiency within a 12-unit inline metamaterial. a-d** Measured power transfer efficiency (η) within the metamaterial at 13.56 MHz, influenced by the number of bends *N* (**a**), diameter of each bend *D* (**b**)**,** winding angle *θ* (**c**), and the salt concentration when immersed in saline (**d**). The efficiency is normalized to the reference condition with no deformation or loading (η_{ref}). The threshold for successful reader-tag connection is assessed by vertically lifting the sensing node (placed at the metamaterial's end) to the highest readable position by the reader placed at the opposite end. VNA near-field probes are then placed at the positions of the reader and the sensing node.

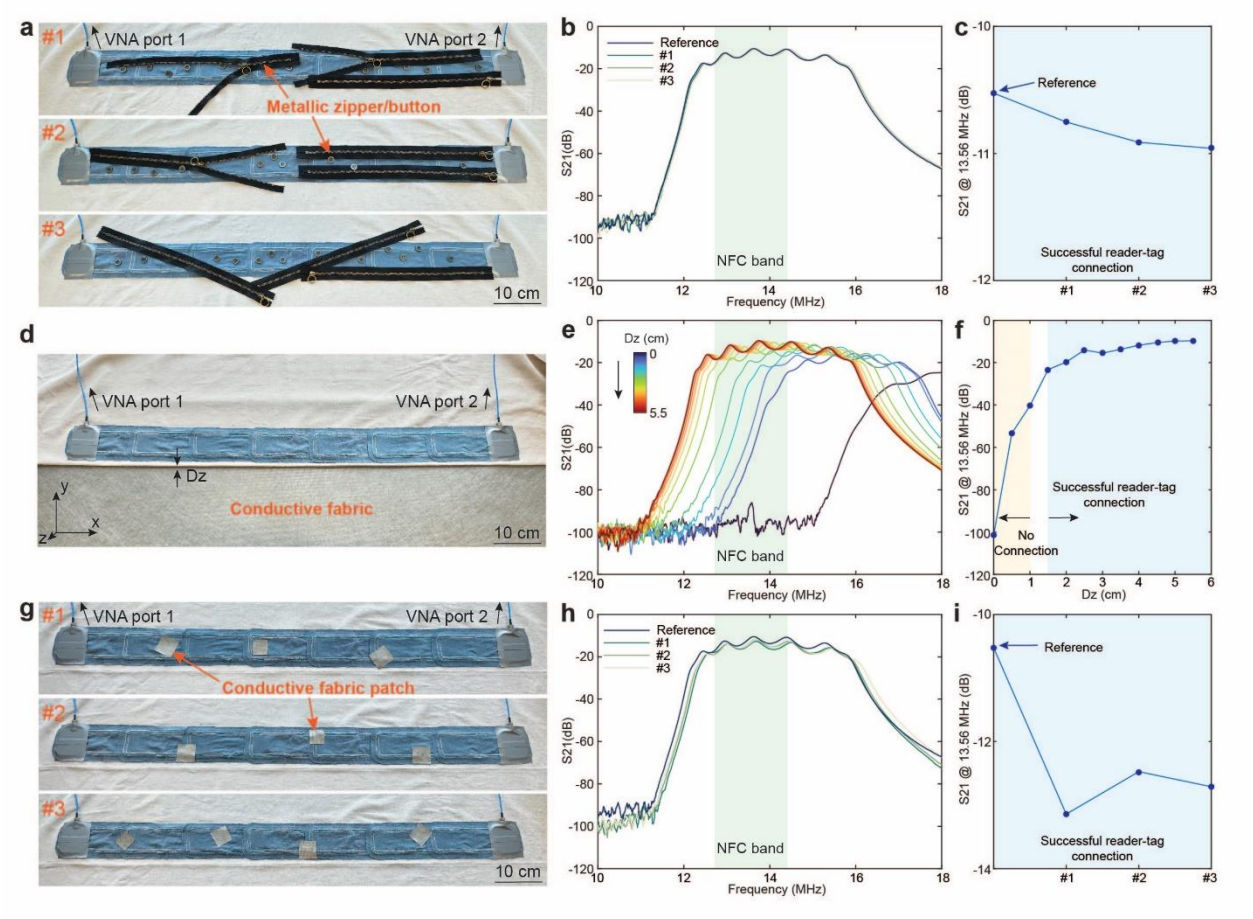

Supplementary Figure 12. **Effects of metallic accessories and conductive fabric. a-c** The 7-unit inline metamaterial is insensitive to the proximity of metallic zippers and buttons (zinc alloy), maintaining a stable transmission profile under three random configurations, with NFC connection preserved when placing a reader and tag at each end of the metamaterial. **d-f** Contact with a piece of conductive fabric (Series 4770, polyester with Copper/Nickle coating, surface resistivity: $< 0.03\Omega/sq$, thickness: 0.19 mm, Holland Shielding Systems BV) covering the entire metamaterial substantially shifts the resonance frequency, disrupting NFC connection until the metamaterial is raised by 1.5 cm vertically. **g-i** The metamaterial demonstrates resilience against smaller conductive fabric patches, showing less significant resonance frequency shifts, and maintains unhindered NFC connection under three random configurations.

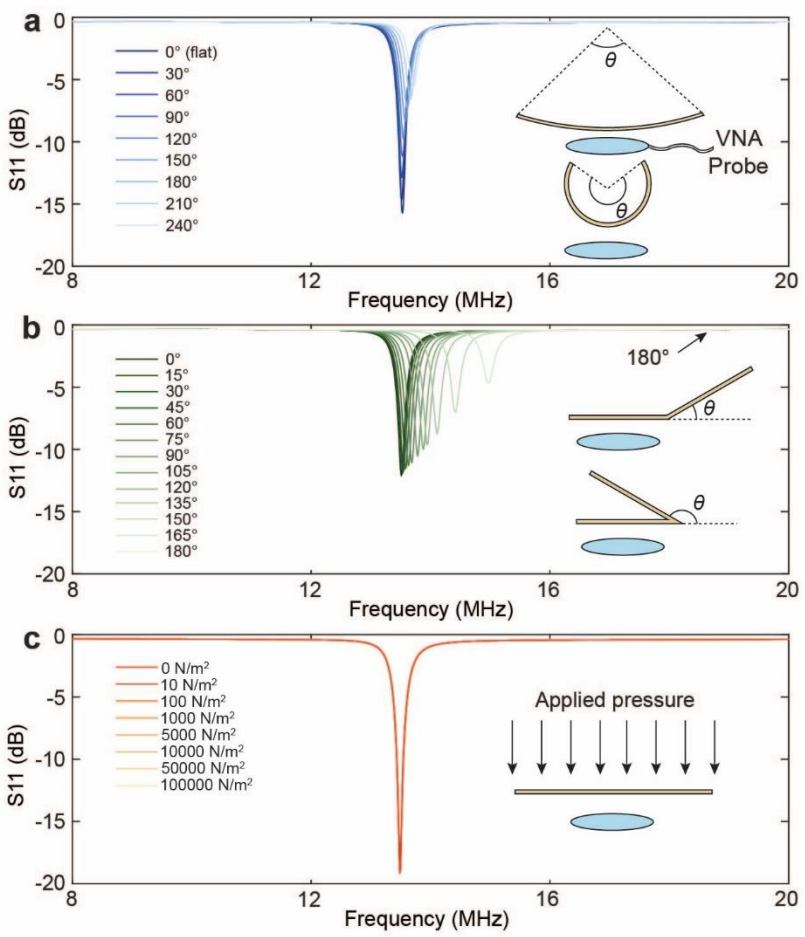

Supplementary Figure 13. Frequency response of the metamaterial unit cell under deformation and pressure. a The unit cell remains spectral stable when flexed to an arc shape, exhibiting only a 1.33% (0.18 MHz) resonance frequency shift when the central angle increases to 240°. **b** Significant frequency shifts occur when the unit cell is folded, due to substantial cancellation of magnetic flux through the resonator loop, emphasizing the need for stretchable joint units at joint positions. **c** The resonance frequency stays stable under pressures up to 100,000 N/m², indicating that such pressure does not cause noticeable deformation or damage to the coaxial cable's internal structure.

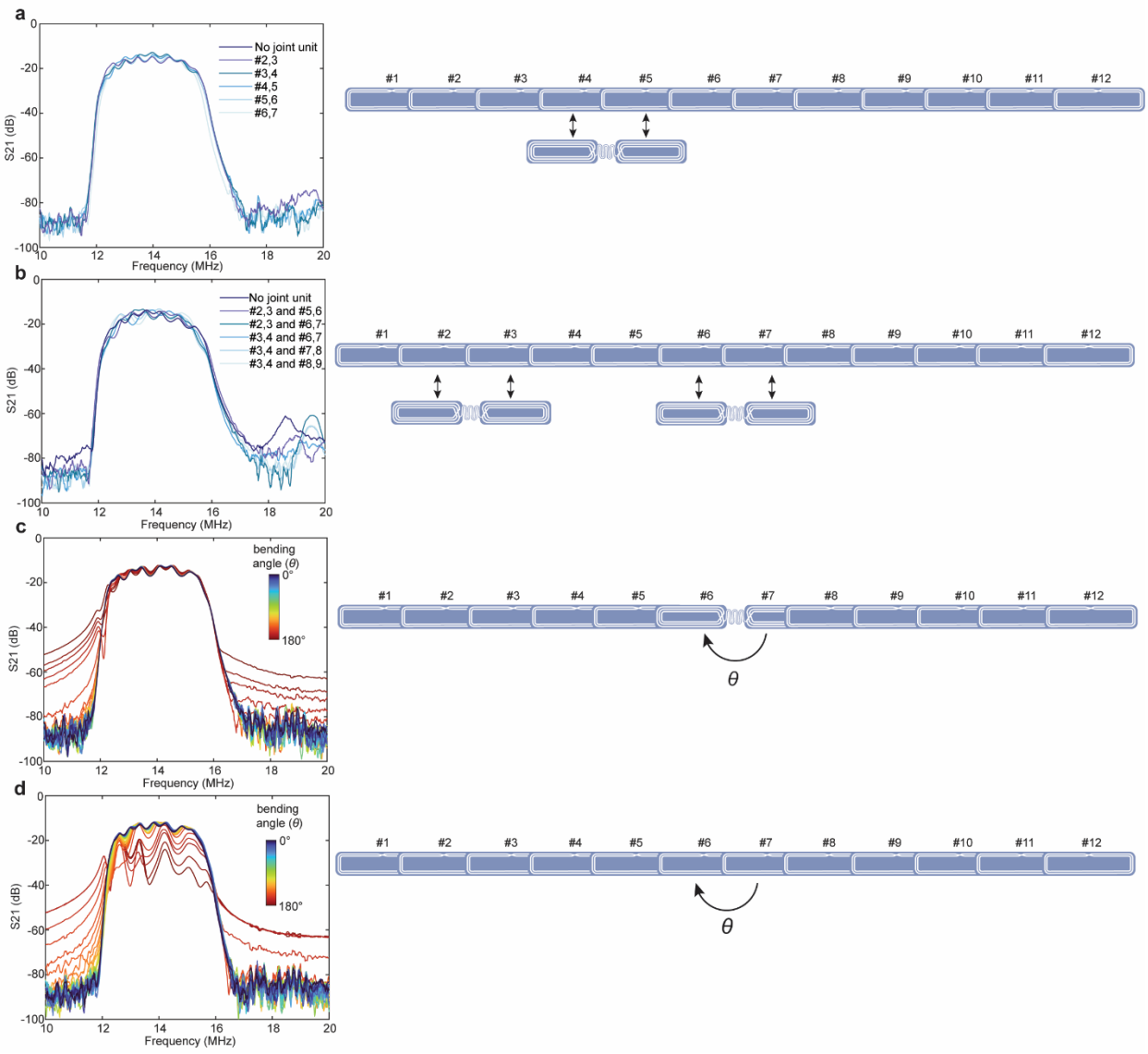

Supplementary Figure 14. Compatibility and stability of the stretchable joint unit when implemented in the BAN. a, b Measured transmission coefficient of a 12-unit inline metamaterial array when replacing certain unit cells with one stretchable unit (**a**) or two stretchable units (**b**). The transmission coefficient remains at the same level while covering the desired NFC passband, highlighting the compatibility of the stretchable join unit that may be implemented at any location in the metamaterial BAN to improve stretchability at joint positions. The parasitic peaks at higher frequencies are induced by the second resonant mode of the joint unit which does not affect NFC signal transmission at 13.56 MHz. **c, d** Measured transmission coefficient of a 12-unit inline metamaterial array while performing bending at the intersection of the 6th and 7th unit cell. When replacing the 6th and 7th unit cells with a joint unit (**c**), the transmission remains at the same level during the bending. When the bending is performed directly on regular unit cells (**d**), the

transmission profile shows fluctuation when the bending is beyond 100°, which is induced by the additional random overlap at the bending position. The additional stretchability from the stretchable joint unit makes the BAN more robust against human motion.

Supplementary Figure 15. NFC tag and reader. a Picture of the fabricated 16 mm × 12 mm circuit board (through PCB milling) of the NFC transponder. **b** NFC tag integrated with a commercial strain sensor and a coaxially-shielded NFC antenna embedded in textile through digital embroidery. **c** Picture of the adopted commercial NFC reader with a 4 cm × 2 cm reader antenna, powered by a USB cable through a laptop.

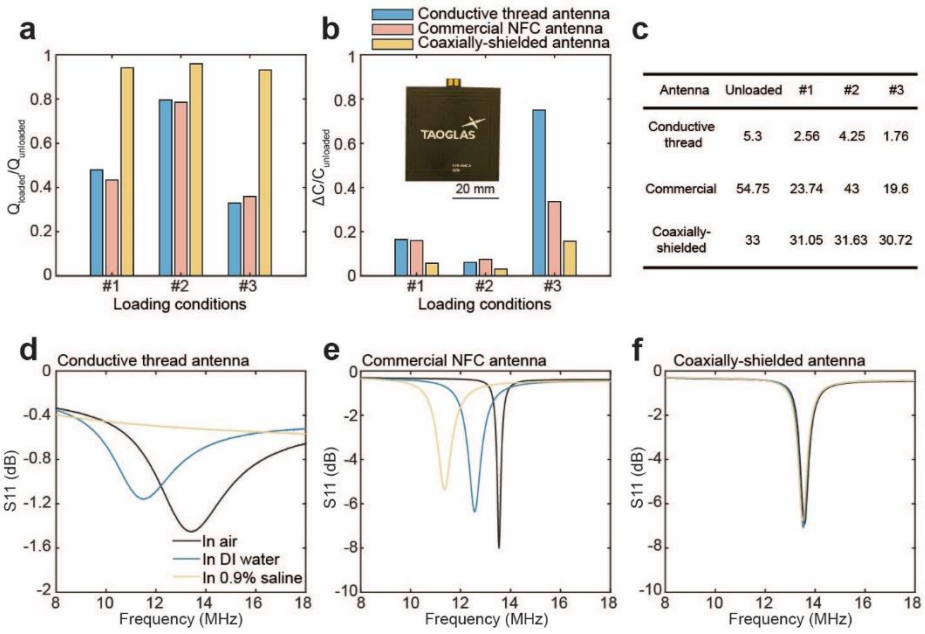

Supplementary Figure 16. Comparison of the coaxially-shielded antenna, conductive thread antenna and commercial flexible NFC antenna. **a** Measured quality factor preservation ($Q_{Loaded}/Q_{Unloaded}$) for the three antennas when affixed to skin (#1), wetted by sweat (#2) and submerged in water (#3). The conductive thread antenna is comparable to the commercial antenna, but both outperformed by the coaxially-shielded antenna. **b** Measured self-capacitance variations $\Delta C/C_{Unloaded}$ for the three antennas. The coaxially-shielded antenna outperforms both the conductive thread antenna and the commercial antenna. Inset: Adopted commercial flexible dual-layered NFC antenna (FXR. 4040. A, 40 mm × 40 mm, Taoglas). **c** Quality factor values as measured in **a**. **d-f** Measured reflection coefficients for the conductive thread antenna (**d**), the commercial NFC antenna (**e**), and the coaxially-shielded antenna (**f**).

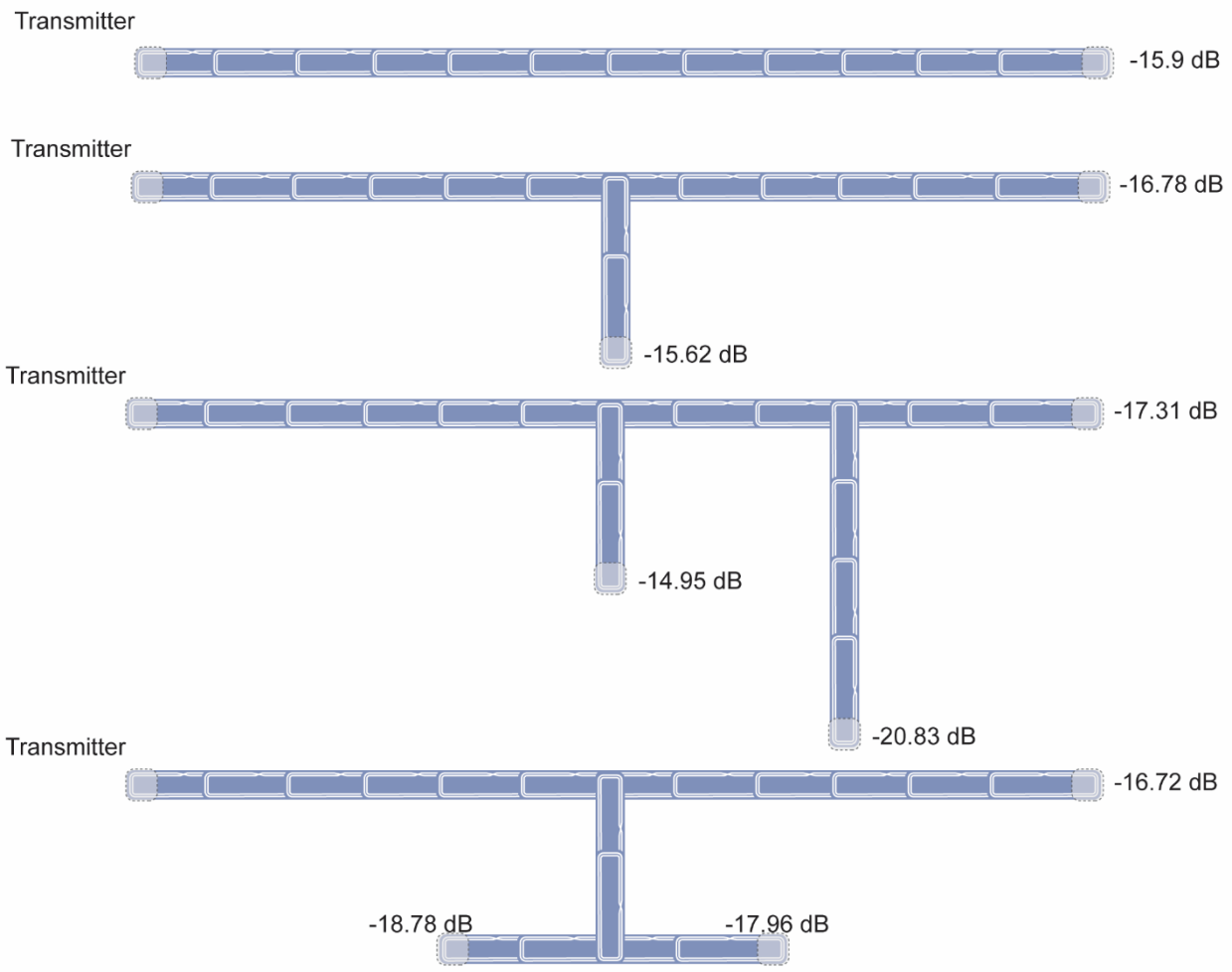

Supplementary Figure 17. Metamaterial arrays branched into separate pathways and the measured transmission coefficient at each terminal.

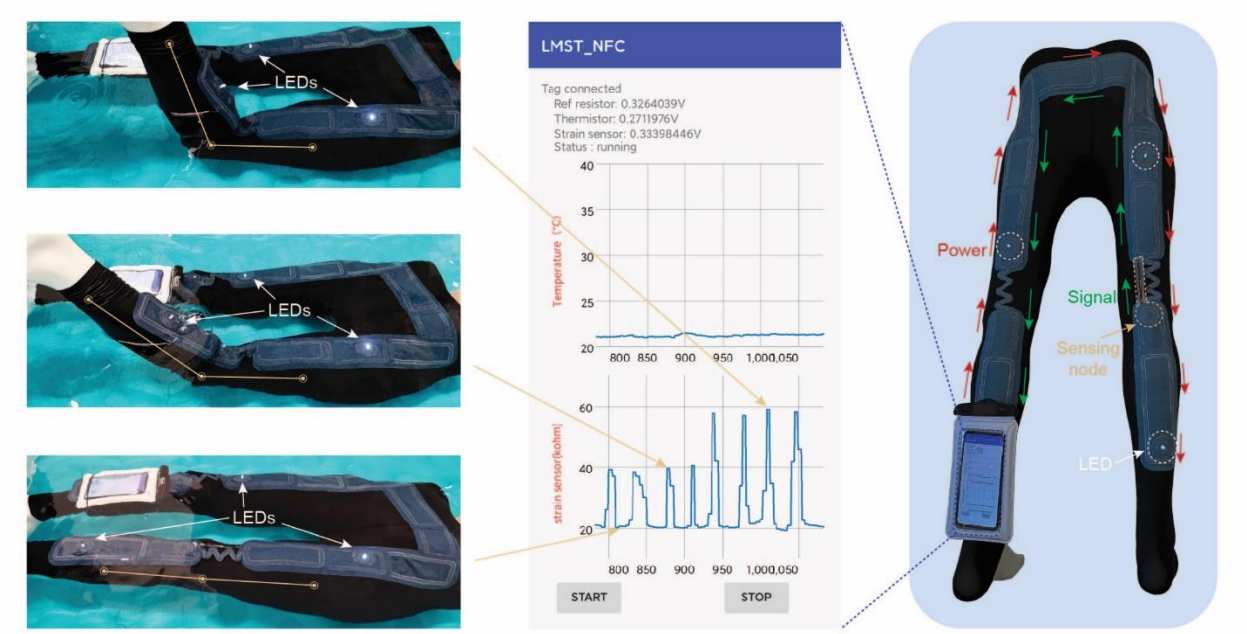

Supplementary Figure 18. Real-time data readout performed underwater. Benefiting from the introduced spectral stability, the metamaterial-enabled BAN promotes reliable underwater real-time data readout. The smartphone, placed in a waterproof pouch, continuously retrieve data from the sensing node, with the strain sensor's resistance indicating the knee flexion, while powering several distant battery-free energy-harvesting LED nodes placed along the BAN.

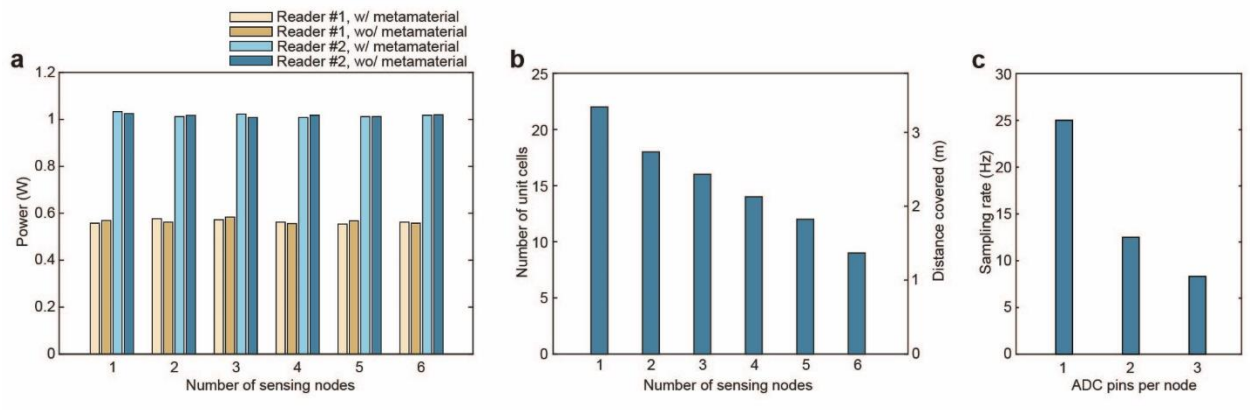

Supplementary Figure 19. Scaling of the BAN's performance with the number of nodes and sensors per node. a Measured power consumption of the adopted reader's circuit board (#1) and an alternative reader's circuit board (ST25R3911B-DISCO, St Microelectronics, #2) while powering different numbers of sensing nodes, with or without the metamaterial. This indicates that the metamaterial enhances the communication range without additional power consumption. **b** The maximum possible number of unit cells in an inline metamaterial array and the distance covered, supporting the associated number of equally spaced sensing nodes. **c** The highest sampling rate for different numbers of ADC pins being sampled in each sensing node.

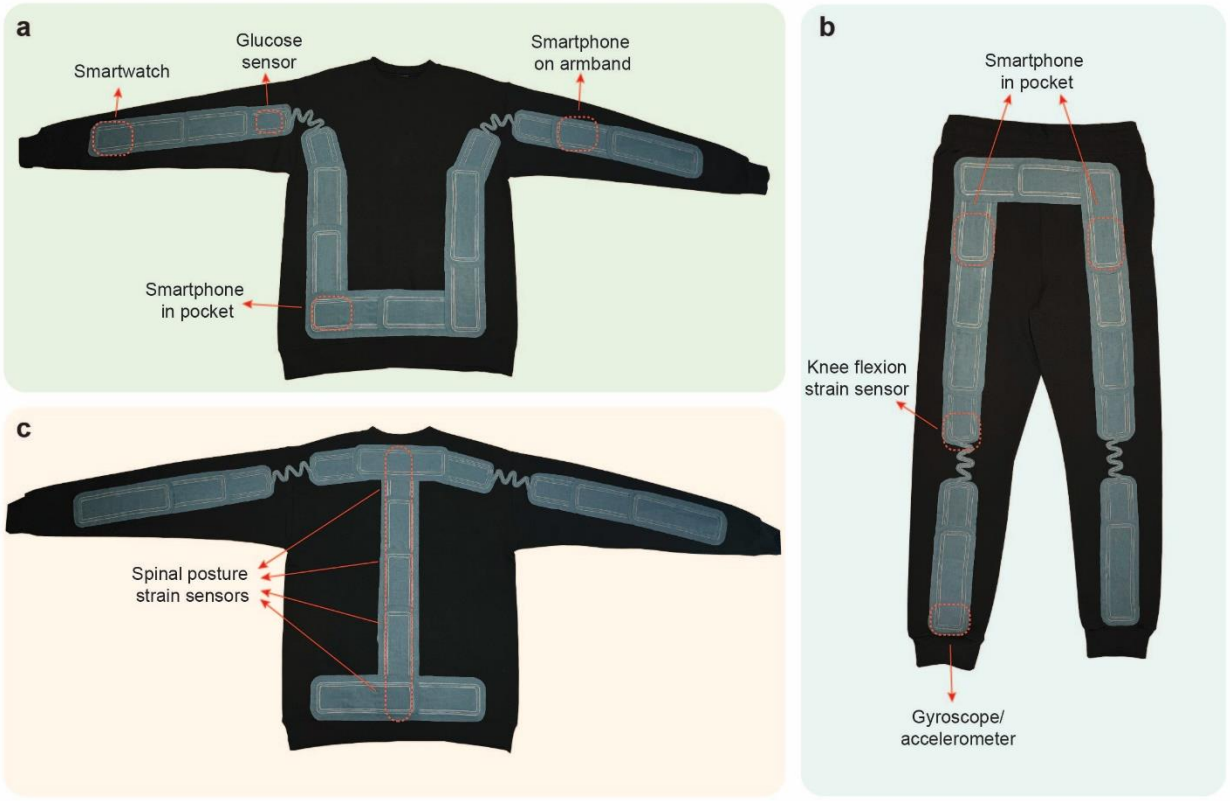

Supplementary Figure 20. Alternative metamaterial patterns with their potential sensing capabilities. a The metamaterial enables continuous blood glucose readings on smartphone or smartwatch from commercial NFC-enabled glucose sensors (e.g., Freestyle Libre 3 by Abbott, recommended to be mounted on the upper arm). **b** The metamaterial can be integrated with strain sensors mounted on the knee to monitor knee flexion, and with a gyroscope/accelerometer mounted on the ankle to monitor stride time and stride time variability. **c** The metamaterial enables placement of strain sensors for spinal posture analysis on any segment of the spine.

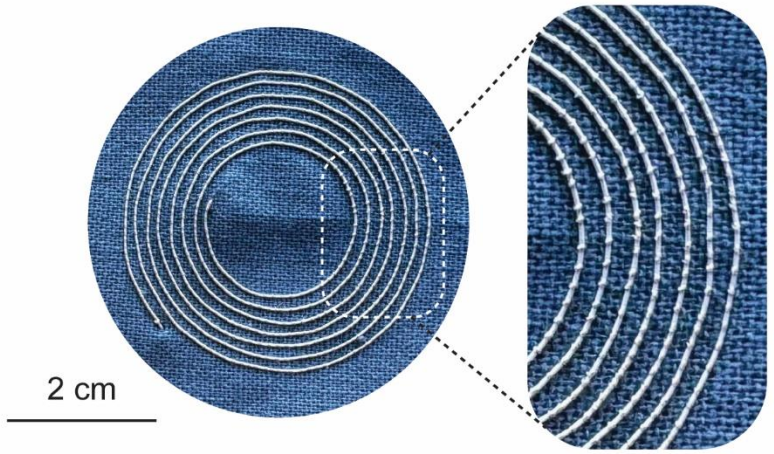

Supplementary Figure 21. Alternative textile metamaterial/antenna construction strategy by directly embroidering commercial micro coaxial cable (9440, Alphawire, cable diameter: 360 µm) on textile. Industry offers micro coaxial cable solutions with diameter as low as 160 µm. Metamaterial/antenna constructed in this way may further reduce the physical footprint of the BAN, but the increased complexity in fabrication and resistive loss must be balanced.

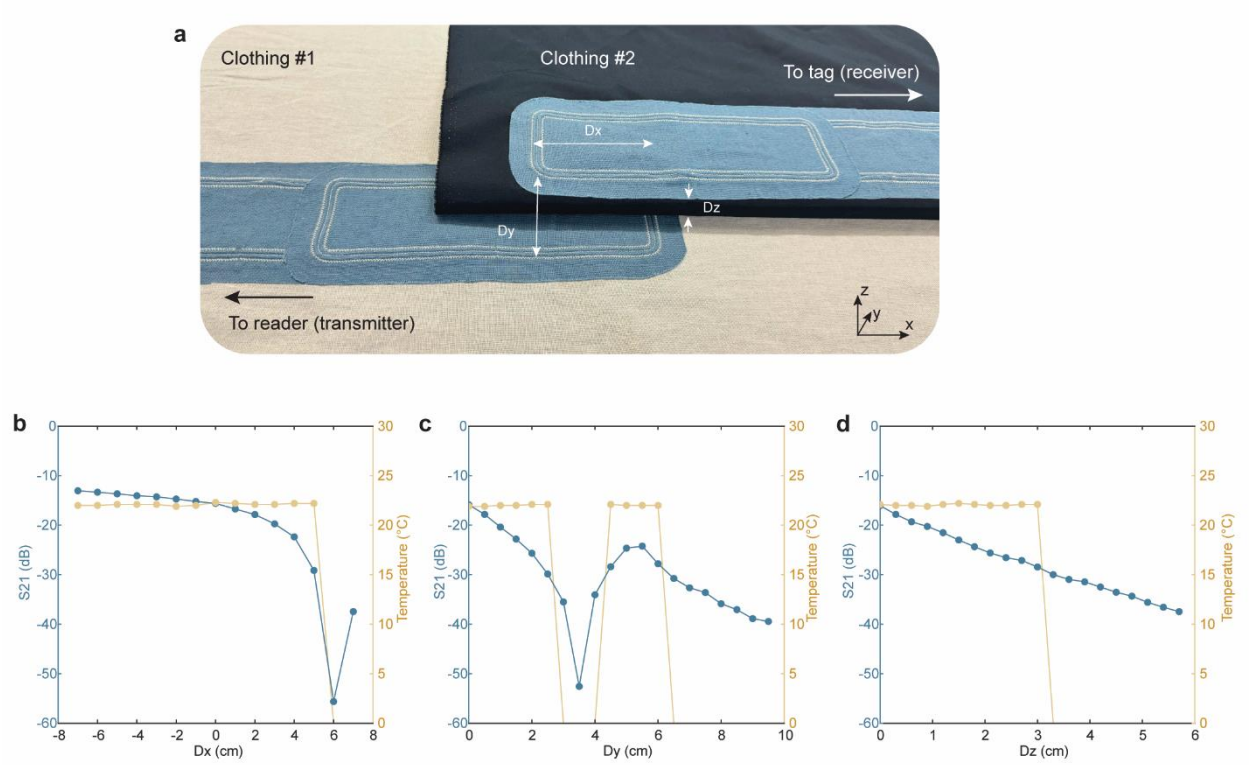

Supplementary Figure 22. Signal transmission across discontinuity between adjacent clothing. a Two 6-unit inline arrays populated on separate clothing may allow the NFC signal to pass the discontinuity between them when placed in proximity to each other. **b, c, d** Measured transmission coefficient of the 12-unit inline metamaterial array (combined by two 6-unit arrays and a discontinuity) when introducing a relative displacement at the discontinuity along the x (**b**), y (**c**), and z (**d**) directions. The initial position is when a 25% overlap is introduced in the x direction. Under each measurement condition, the transmitter and receiver loops are replaced with the NFC reader and tag to conduct a temperature measurement. A 0°C measurement indicates the tag can not be detected by the reader. The BAN offers flexibility for displacement between clothing, and displacement along the y and z direction may be compensated by a higher overlap along the x direction.

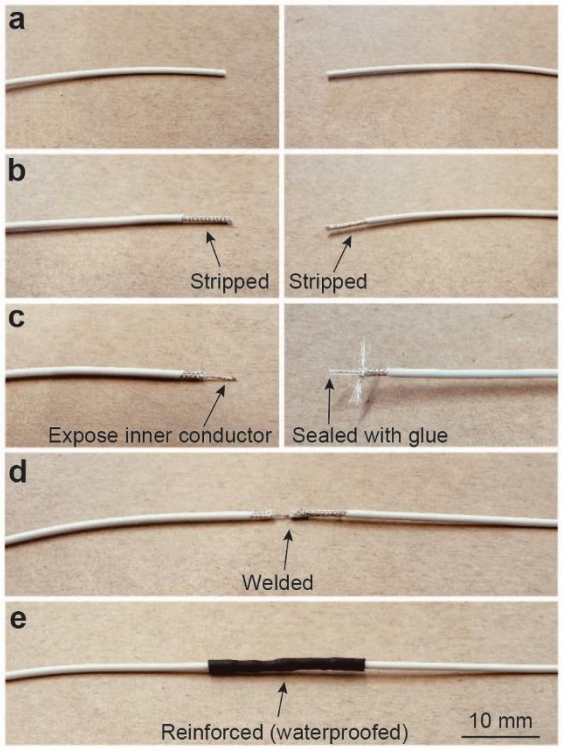

Supplementary Figure 23. **Step-by-step demonstration for constructing a coaxially-shielded resonator at the open slit. a** Two ends of a cable segment. **b** The jacket is stripped to expose the outer conductor. **c** The outer conductor and insulation are stripped to expose the inner conductor on the left; the end of the inner conductor is sealed with glue to prevent short circuits on the right. **d** The inner conductor on the left is welded to the outer conductor on the right. **e** The open slit is reinforced with a waterproof heat shrink tubing.

Supplementary Figure 24. Alternative textile NFC antenna designs by leveraging the programmable digital embroidery patterns. **a** Antenna with the same size as the metamaterial, potentially integrated into the BAN to serve as both a tag (receiver) and transmission relay simultaneously. **b** Antenna with larger size for increased operation range. **c** A round antenna with more turns and higher filling ratio to eliminate the use of tuning capacitor.

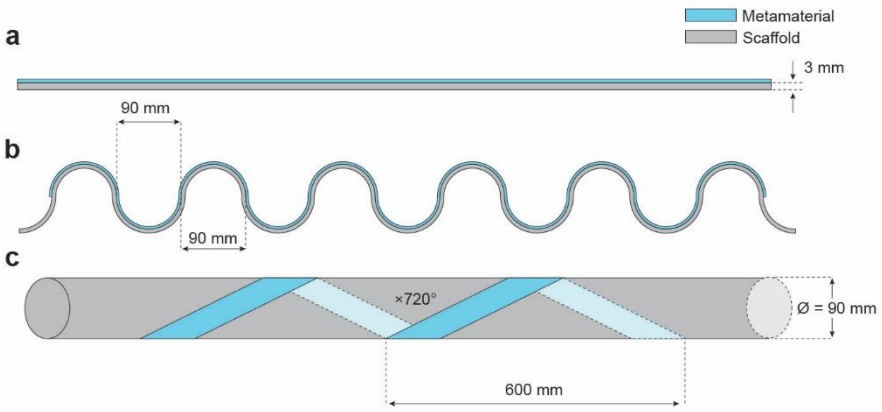

Supplementary Figure 25. **Experimental setup adopted in Figure 2e-g. a** In Fig. 2e, the metamaterial was placed on an acrylic board. **b** In Fig. 2f, the metamaterial was placed on a 3D-printed serpentine PLA scaffold. **c** In Fig. 2g, the metamaterial was wound around an acrylic pipe.

Supplementary Table 1. Comparison of recent textile BAN technologies.

Reference	This work	S1	S2	S3	S4	S5
Wireless communication technology	NFC (13.56 MHz)	NFC (13.56 MHz)	NFC (13.56 MHz)	NFC (13.56 MHz)	Bluetooth (2.4 GHz)	Modified RFID & Bluetooth
Signal transmission	MI surface wave	Conductive relay	Conductive relay	MI surface wave	Surface plasmon	Radiative (over the air)
Sampling rate	Up to 25 Hz (26.48 kbps data rate)	Up to 8 Hz (26.48 kbps data rate)	Up to 12 Hz (26.48 kbps data rate)	Up to 32 Hz (26.48 kbps data rate)	Up to 1 Mbps data rate	Up to 4 Mbps data rate
Composition of signal transmission relay	Off-the-shelf coaxial cable	Encapsulated conductive thread	Liquid metal tube	Copper/aluminum foil	Off-the-shelf conductive fabric	No relay (over the air)
Clothes integration	Washable hemming tape	Irreversible Embroidery	Irreversible Embroidery	Heat-transferred vinyl	Fabric adhesive	Double-sided tape
Reader/sensor placement	Up to user	Pre-determined terminal/hub	Pre-determined terminal/hub	Up to user	Up to user	Up to user (each sensor require separate initiator)
Measures for improved spectral stability	Coaxially-shielded internal structure	NO (spiral inductive pattern)	NO (spiral inductive pattern)	Ground layer (spiral inductive pattern)	No (harnessed the sensitivity for sensing capability)	NO (spiral inductive pattern)
Sensitivity to water immersion	Insensitive (coaxially-shielded)	Sensitive	Sensitive	Sensitive	Sensitive	Sensitive
Washability	Multiple machine-washing	Unclear	Multiple machine-washing	20-min hand-washing	Unclear	Can be removed during washing

References

[S1] Lin, R., et al. Wireless battery-free body sensor networks using near-field-enabled clothing. *Nat. Commun.* **11**, 444 (2020).

[S2] Lin, R., et al. Digitally-embroidered liquid metal electronic textiles for wearable wireless systems. *Nat. Commun.* **13**, 2190 (2022).

[S3] Hajiaghajani, A., et al. Textile-integrated metamaterials for near-field multibody area networks. *Nat. Electron.* **4**, 808-817 (2021).

[S4] Tian, X., et al. Wireless body sensor networks based on metamaterial textiles. *Nat. Electron.* **2**, 243-251 (2019).

[S5] Niu, S. et al. A wireless body area sensor network based on stretchable passive tags. *Nat. Electron.* **2**, 361–368 (2019).